

A Straight Forward Method to Read the Nuclear Qudit of $4f$ Single-Molecule Magnets : $^{163}\text{DyPc}_2$

Hongyan Chen,^{1,*} Simon Gerber,^{1,*} Philip Schmid,¹ Nola Warwick,¹ Charanpreet Singh,¹ Svetlana Klyatskaya,² Eufemio Moreno-Pineda,^{3,4} Mario Ruben,^{3,2,5} and Wulf Wulfhekel^{1,3}

¹*Physikalisches Institut, Karlsruhe Institute of Technology (KIT), 76131 Karlsruhe, Germany*

²*Institute of Nanotechnology, Karlsruhe Institute of Technology (KIT), 76344 Eggenstein-Leopoldshafen, Germany*

³*Institute of Quantum Materials and Technologies (IQMT), Karlsruhe Institute of Technology (KIT), Hermann-von-Helmholtz-Platz 1, D-76344, Eggenstein-Leopoldshafen, Germany*

⁴*Universidad de Panamá, Facultad de Ciencias Naturales,*

Exactas y Tecnología, Depto. de Química-Física, 0824 Panamá, Panamá

⁵*Centre Européen de Sciences Quantiques (CESQ) in the Institut de Science et d'Ingénierie Supramoléculaires (ISIS), 8 allée Gaspard Monge BP 70028, 67083 Strasbourg Cedex France*

(Dated: March 16, 2026)

Nuclear spins in $4f$ single-molecule magnets (SMMs) are promising qubits or qudits candidates for quantum information processing due to their relative isolation and reduced susceptibility to environmental disturbances, while hyperfine coupling with the $4f$ moments enables readout and control. So far, the nuclear spin states of individual TbPc_2 SMMs have been detected in transport measurements via the spin-cascade effect, in which transitions of the Tb^{3+} magnetic moment coupled to the unpaired ligand electron manifest as conductance jumps in spin-polarized transport. The ligand electron also gives rise to a Kondo effect through its interaction with the metallic contacts. By sweeping a magnetic field along the easy axis of the Tb^{3+} moment, the system is tuned to avoided crossings of the hyperfine levels, such that the magnetic field at which the conductance jumps occur indicates the nuclear spin state. Here, we present a method to read the nuclear spin of $^{163}\text{DyPc}_2$ ($I = 5/2$) using millikelvin spin-polarized scanning tunneling microscopy without the need for magnetic-field sweeps. Instead, hyperfine interactions modify the statistics of the telegraph noise generated by reversals of the Dy^{3+} moment, thereby revealing the nuclear spin state. We observe nuclear spin relaxation times T_1 in excess of minutes at 35 mK. Furthermore, we drive nuclear spin transitions using a radio-frequency field and detect the resulting nuclear magnetic resonance directly in the tunneling current, as the conductance near the split Kondo peaks depends on the nuclear spin state.

Quantum computation with single spins requires conflicting conditions, i.e., the quantum spin should be isolated from the bath to ensure long lifetimes and coherence times, while still allowing control and readout via external stimuli[1–11]. A particularly successful approach is the so-called spin cascade in metal-organic molecules, in which the qubit or qudit (a quantum system with more than two states) is encoded in the nuclear spin I of a rare-earth ion [8]. The coupling to the external world is mediated by the hyperfine interaction with the electronic total angular momentum J of the rare-earth ion, which is in turn exchange-coupled to a single electron spin S on the organic ligands of a phthalocyanine (Pc) double-decker molecule [12]. This unpaired electron undergoes Kondo screening when the molecule is placed on a conductive surface [13–15]. In Au break-junctions, this mechanism has been used to read, write and manipulate the nuclear spin of TbPc_2 [8, 12] and the Grover's algorithm has been realized [16–18]. To read out the nuclear spin, the gate voltage was tuned to match the Kondo resonance while sweeping the magnetic field normal to the Pc ligands. This drives a transition of the ion's total angular momentum at the avoided level crossings of the hyperfine-split states, thereby revealing the nuclear spin state [8, 12]. The transition of J in TbPc_2 observed in

the conductance is feasible because Tb^{3+} , with its integer number of electrons, is a non-Kramers system, leading to avoided level crossings of the hyperfine levels at specific external magnetic fields. The measurement therefore constitutes a projective measurement of the nuclear spin.

In this work, we take an alternative approach using the same spin cascade, but based on a Kramers system. We demonstrate a readout scheme for the nuclear spin states of the $4f$ single-molecule magnet $^{163}\text{DyPc}_2$ using spin-polarized scanning tunneling microscopy (Sp-STM) at around 35 mK, without requiring magnetic-field sweeps. The basic idea of the scheme is shown in Fig. 1. $^{163}\text{DyPc}_2$ molecules were deposited onto a clean Au(111) surface by sublimation [19–24]. In STM images they exhibit the characteristic cloverleaf structure of the top Pc ligand (Fig. 1a) [13, 25]. Owing to the energy-level alignment with the Au(111) work function, the upper ligand hosts a single electron forming a singly occupied molecular orbital (SOMO) [26]. This unpaired electron is Kondo-screened by the substrate and exchange-coupled to the magnetic moment of the Dy^{3+} ion. This exchange interaction acts as an effective magnetic field on the SOMO electron, splitting the Kondo resonance into two spin-polarized peaks and thereby encoding the orientation of the Dy^{3+} total angular momentum (J) in the electronic

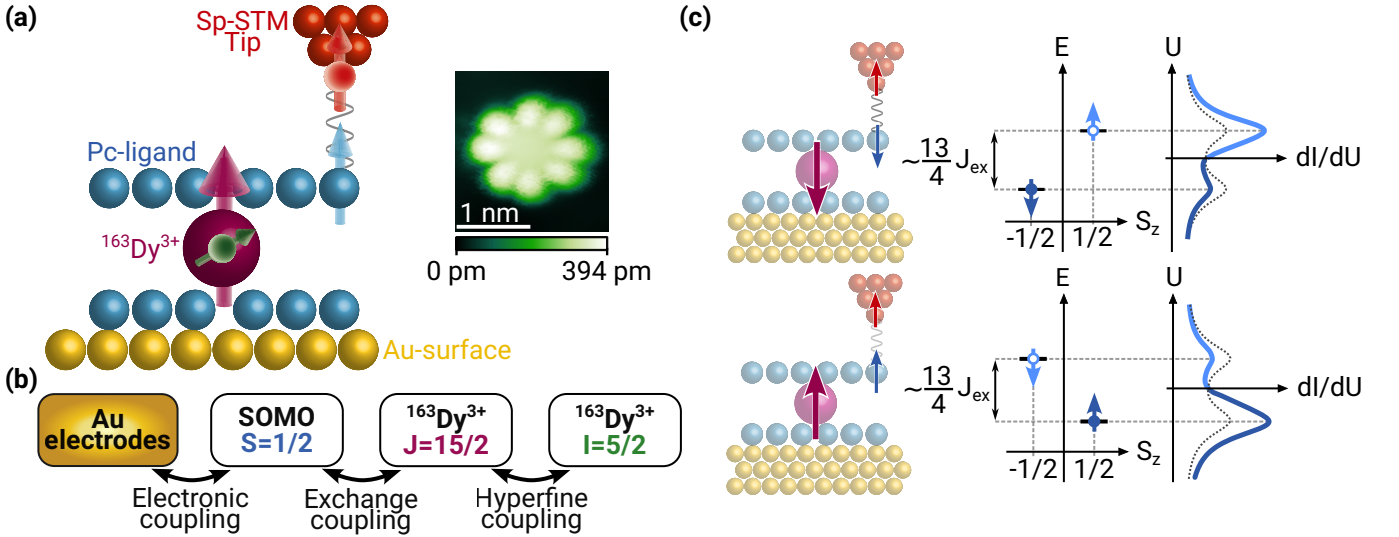


Figure 1. Readout principle based on the spin cascade. (a) Schematic side view of a $^{163}\text{DyPc}_2$ molecule measured by a spin-polarized tip, together with an STM topography of a DyPc_2 molecule on Au (111) (1 V, 20 pA). The spin-polarized STM tip (tip magnetization indicated by a red arrow) senses the ligand spin (blue arrow), which is exchange-coupled to the Dy^{3+} total angular momentum (purple arrow); this, in turn, is hyperfine-coupled to the nuclear spin (green arrow). (b) Scheme of the resulting spin cascade, illustrating the electronic, exchange, and hyperfine couplings. (c) STM measurement principle. Energy splitting of the ligand spin states and the resulting spin-polarized differential conductance spectra for two orientations of Dy^{3+} momentum.

state of the SOMO (S). The Dy^{3+} electronic moment is in turn hyperfine-coupled to the nuclear spin (I), allowing the nuclear spin state to be accessed through this cascade of electronic, exchange, and hyperfine interactions via the spin-polarized Kondo resonance detected by spin-polarized STM.

The first part of this cascade, namely the readout of the Dy^{3+} electronic moment J , has been demonstrated in our previous work [25]. The corresponding STM measurement principle is illustrated in Fig. 1c. Depending on the orientation of the Dy^{3+} moment ($J_z = \pm 13/2$) the two spin states of the unpaired electron ($S_z = \pm 1/2$) are exchange-split by $\pm \frac{13}{4} J_{\text{ex}}$, resulting in fully spin-polarized Kondo peaks [25, 27, 28]. Owing to the tunneling magnetoresistance effect (TMR) [29], the differential conductance of the occupied and unoccupied Kondo peaks depends on the magnetic orientation of the Dy^{3+} moment. This dependence allows the orientation of the Dy^{3+} magnetic moment to be determined by spin-polarized scanning tunneling spectroscopy (STS).

Using this principle, the magnetization curve of $^{164}\text{Dy}^{3+}$ without nuclear spin as a function of an external magnetic field applied normal to the surface (Fig. 2a) was previously determined [25]. The magnetization shows no remanence and vanishes at zero field. This behavior originates from quantum tunneling of magnetization (QTM) caused at an avoided level crossing between the two lowest-energy states of the coupled Dy-ligand spin system, $|S_z, J_z\rangle = |+1/2, +13/2\rangle$ and $|-1/2, -13/2\rangle$. The avoided level crossing results from mixing terms of

the Stevens operators describing the crystal field splitting [30–32]. Because the total angular momentum of the coupled Dy–ligand system is integer, the ground state is not protected by Kramers degeneracy.

Introducing the nuclear spin $I = 5/2$ in $^{163}\text{DyPc}_2$ qualitatively changes the situation. The hyperfine interaction between the Dy^{3+} total angular momentum and the nuclear spin shifts the energies of the electronic states depending on the nuclear spin projection. As a result, the magnetization curve of the Dy^{3+} ion is shifted for different nuclear spin orientations, leading to finite expectation values of the Dy^{3+} magnetization even at zero external magnetic field. Consistent with this picture, a finite Dy^{3+} magnetization at zero magnetic field can be experimentally observed, as shown in Fig. 2b. The corresponding states remain stable for tens of minutes and exhibit a clear spin polarization of the split Kondo peaks.

To better understand the microscopic origin of this behavior, the effective spin Hamiltonian of the $^{163}\text{DyPc}_2$ molecule is considered.

$$\begin{aligned}
 \hat{H} = & B_2^0 \hat{O}_2^0 + B_2^2 \hat{O}_2^2 + B_4^0 \hat{O}_4^0 + B_4^4 \hat{O}_4^4 + B_6^0 \hat{O}_6^0 + B_6^4 \hat{O}_6^4 \\
 & + A_{IJ} \hat{\mathbf{I}} \cdot \hat{\mathbf{J}} \\
 & + P \left\{ \hat{I}_z^2 - \frac{1}{3} I(I+1) \right\} \\
 & + g_J \mu_B \hat{\mathbf{J}} \cdot \mathbf{B} + g_S \mu_B \hat{\mathbf{S}} \cdot \mathbf{B} + g_I \mu_B \hat{\mathbf{I}} \cdot \mathbf{B} \\
 & - J_{\text{ex}} \hat{\mathbf{J}} \cdot \hat{\mathbf{S}}
 \end{aligned} \tag{1}$$

Here, $\hat{\mathbf{S}}$ denotes the ligand spin operator with spin quan-

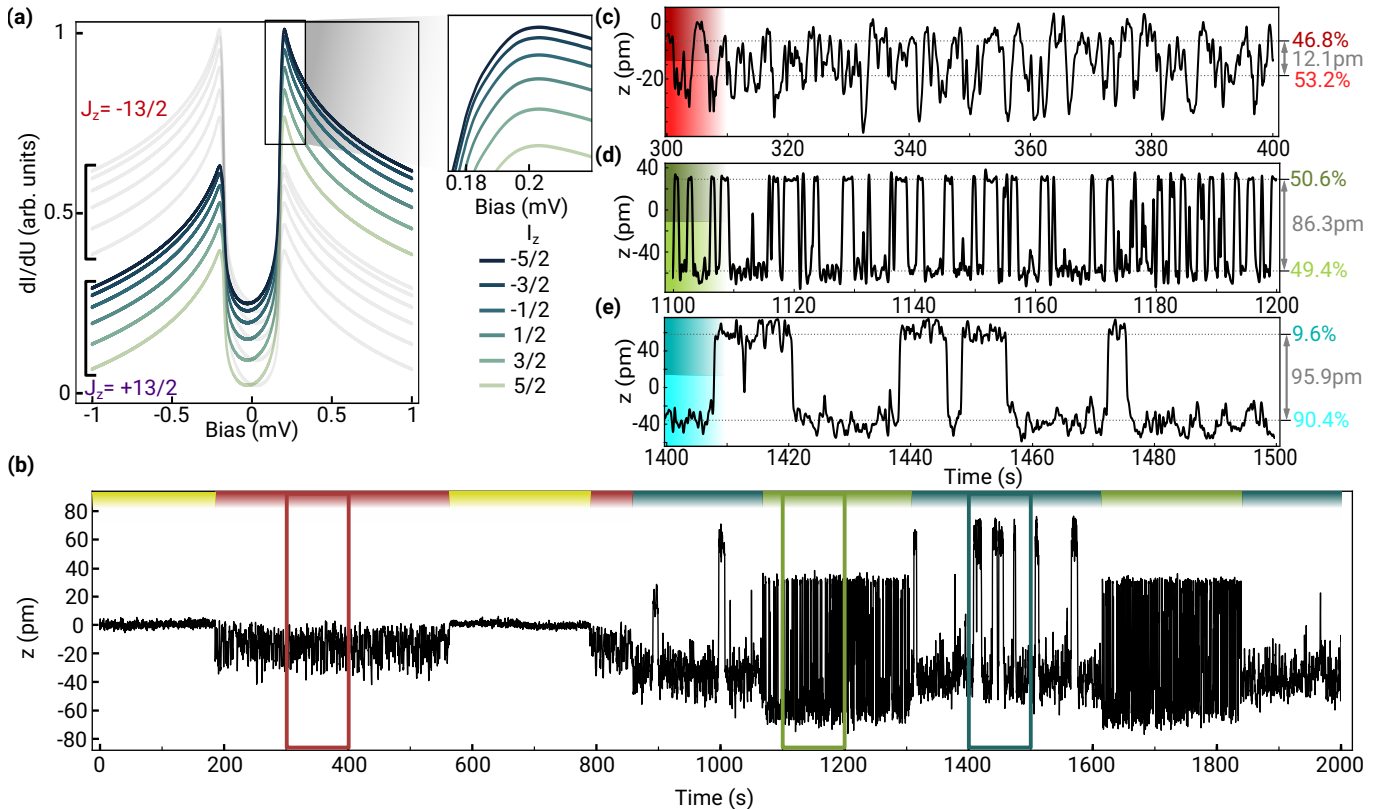
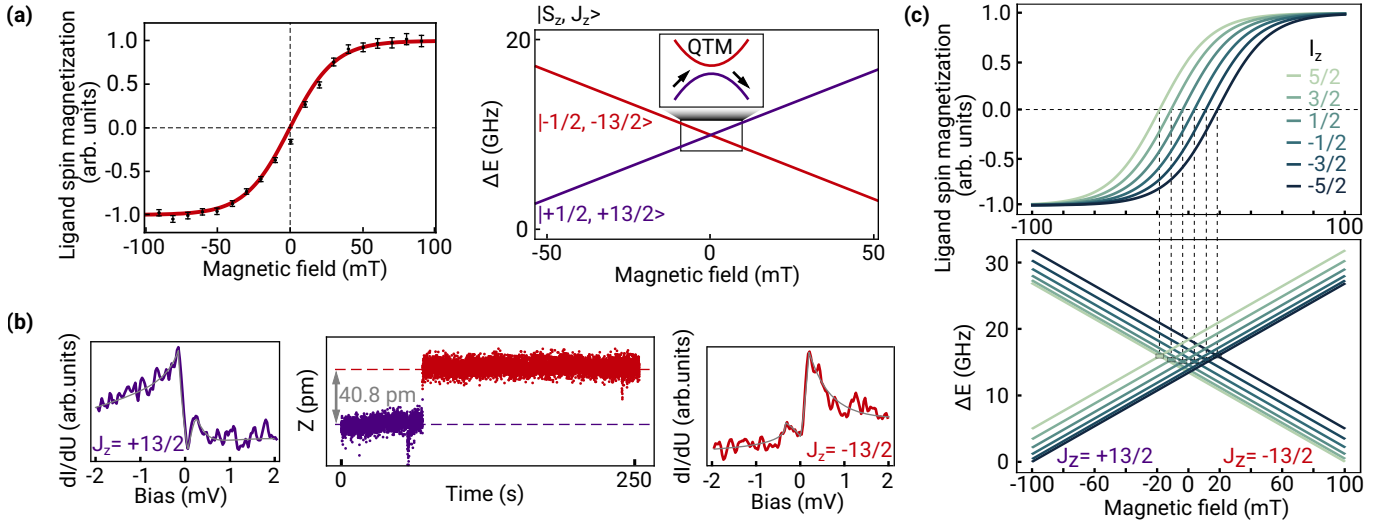


Figure 3. Z-position changes of the tip represent conductance height changes at Kondo peak (a) Expected differential conductivity with 30% spin polarization for different quantum states (b) Time trace of the tip z-position on top of a $^{164}\text{DyPc}_2$ molecule. The signal shows colored sections that differ in their behavior. (c)-(e) Zoomed in plots for the colored sections with population and jump height.

tum number $S = 1/2$, $\hat{\mathbf{J}}$ the Dy³⁺ total angular momentum operator with $J = 15/2$, and $\hat{\mathbf{I}}$ the nuclear spin operator of ¹⁶³Dy with $I = 5/2$. J_{ex} describes the exchange interaction between \hat{S} and \hat{J} . \hat{O}_n^m and B_n^m are the Stevens operators and the corresponding crystal-field parameters of DyPc₂ taken from Ref. [23, 33]. The parameters reflect a DyPc₂ molecule of C_{2v} symmetry. A and P denote the hyperfine and quadrupole parameters of ¹⁶³DyPc₂ [19] (see Supplemental Material).

Using this Hamiltonian, the low-energy Zeeman diagram of the coupled ligand-Dy-nuclear spin system around zero magnetic field is calculated, shown in Fig. 2c. The two ground-state branches, $J_z = \pm 13/2$, are each split into six different sublevels by the hyperfine coupling to the nuclear spin $I = 5/2$. Around zero magnetic field, the eigenstates remain essentially unmixed and are nearly pure in the z components of the individual spins, since the exchange and quadrupole terms do not mix the corresponding z -eigenstates. Only a minute mixing arises from the non-diagonal crystal-field terms \hat{O}_2^2 and \hat{O}_4^4 , which also generate avoided level crossings at finite fields. This level structure explains the stability of the Dy³⁺ magnetization observed at zero field in Fig. 2b and provides the microscopic basis for nuclear-spin-dependent electronic states.

The splitting of the Kondo resonance peaks originates from the exchange interaction between the Kondo-screened ligand spin and the Dy³⁺ magnetic moment. As the energies of the states involved in Kondo screening are further modified by the hyperfine interaction with the nuclear spin, the shape of the Kondo peaks depends on the nuclear spin orientation. This provides a direct spectroscopic pathway to probe the nuclear spin state.

To quantify this effect, the expected differential conductivity dI/dU using the third-order perturbation model developed by Ternes for spin-flip scattering in spin-polarized STM spectroscopy is calculated [34]. In this approach the transition probabilities for tunneling electrons to induce changes of the ligand spin, the Dy³⁺ total angular momentum and the nuclear spin are computed.

The calculated transition probabilities show that processes involving changes of the nuclear spin are seven orders of magnitude less probable already for first order processes, and are therefore irrelevant on the level of the present third-order treatment. This suppression arises because the eigenstates are nearly pure in the individual spin projections, i.e., the corresponding spin operators almost commute with the Hamiltonian. Consequently, the tunneling interaction induces almost exclusively spin-flip transitions of the ligand spin. The Dy³⁺ moment and the nuclear spin therefore remain effectively stable and do not scatter with conduction electrons, in agreement with the experimental observations [12]. The simulations of the Kondo spectra were thus based on spin transitions of the ligand spin alone.

Figure 3a shows the calculated differential conductance

dI/dU for the different nuclear spin projections I_z , exhibiting the characteristic shape of a split Kondo resonance of the ligand spin. As can be seen from the figure, different nuclear spin projections lead to slightly shifted peak positions and modified peak intensities. The former originates from the small hyperfine and dipolar fields acting on the Dy³⁺ moment, while the latter arises because the energy of the localized spin in the Kondo model, i.e. the Anderson impurity states, depends on the nuclear spin projection, which changes the local density of states of the Kondo resonance.

To probe these nuclear-spin-dependent spectral features experimentally, spin-polarized STM measurements are performed at a bias voltage near one of the maxima of the split Kondo peak, where the small peak shifts and intensity variations predicted in Fig. 3a can be detected most sensitively. Under constant current feedback at a bias voltage of the maximum of the split Kondo peak, only the states between the Fermi level and the bias voltage contribute to tunneling. A change of the local density of states (LDOS) in this energy window induces changes of the z -position of the STM tip in the constant current feedback mode. Comparing the spectra of the molecule and the substrate reveals that a reversal of the Dy³⁺ moment changes the differential conductance by the factor of the tip spin-polarization as the Kondo peaks are fully spin-polarized. The feedback loop will thus change the z -position of the tip by several tens of pm, making it easy to detect the quantum state of the DyPc₂ molecule. Changes of the nuclear spin state induce smaller changes, as they do not affect the spin-polarization of the split Kondo peaks.

Figure 3b shows the corresponding time trace of the STM tip height measured on the Pc ligand at a bias voltage of 240 μV near the maximum of the split Kondo peak and at vanishing external magnetic field. The time trace reveals telegraph noise with clearly different switching behaviors in different time intervals. Therefore, the trace is divided into four distinct regions, highlighted by the colored sections in Fig. 3b and shown in detail in Fig. 3c-e.

On short time scales, the signal exhibits telegraph noise switching between two states arising from reversals of the Dy³⁺ magnetic moment, producing large changes in the STM tip height. Applying a magnetic field of only 50 mT normal to the sample surface suppresses these jumps, confirming their magnetic origin.

On longer time scales, however, the switching behavior evolves. These slow variations originate from changes of the nuclear spin, which modify the effective magnetic field acting on the Dy³⁺ moment through the hyperfine interaction. Depending on the nuclear spin orientation, the system is at different distances (in magnetic field) from the avoided level crossings, resulting in different switching rates of the Dy³⁺ moment.

The yellow region corresponds to a very stable config-

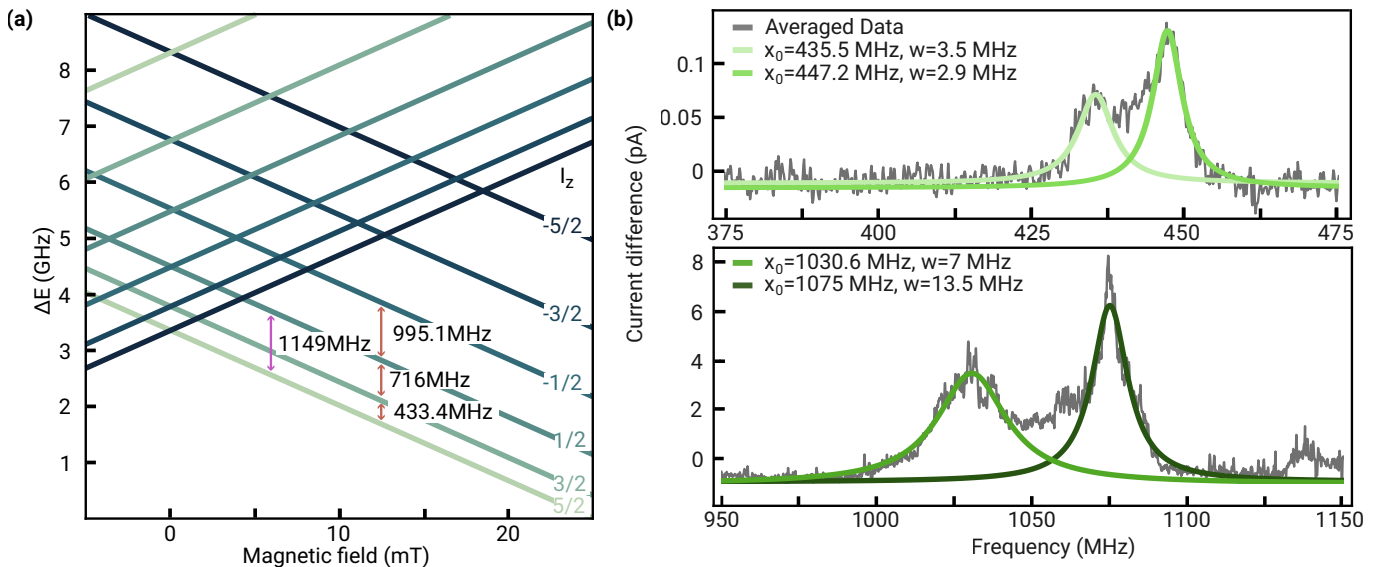


Figure 4. Manipulation with RF signal (a) Zoomed in Zeeman graph with frequencies of dipole and quadrupole direct transitions. (b) Measured difference in current for dipole transitions.

uration in which no Dy^{3+} spin flips occur because the avoided level crossing lies far from the applied field. In the blue region (Fig. 3e), the switching rate increases as the hyperfine field brings the system closer to the avoided level crossing, resulting in a strongly asymmetric population of the two states and most of the time in the low-conductance state. In the green region (Fig. 3d), the switching rate increases further and the populations of the two states become nearly balanced. In the red region (Fig. 3c), the switching rate is highest and approaches the bandwidth limit of the feedback loop, indicating that the system is closest to the avoided level crossing. Transitions between these regions occur on much longer time scales, consistent with the long lifetime of the nuclear spin states.

The z -position of the STM tip in the telegraph noise are also altered by changes in the nuclear spin, in accordance with variations in LDOS associated with different nuclear spin states. Given the reduced magnitude of these LDOS variations, the resulting height changes are significantly less than those induced by the switching of the Dy^{3+} magnetic moment. At very high switching rates, the finite bandwidth of the feedback loop restricts measurable height changes even further (see Fig. 3c). The expected changes of the z -position due to changes of the LDOS on the level of 10% caused by the nuclear spin orientation are of the order of 10 pm, in agreement with the experimental observation.

This experimental protocol therefore allows us to determine the Dy^{3+} nuclear spin orientation from the conductance, or equivalently from z -position, measured at the Kondo peak. We note that although tunneling electrons induce fluctuations of the ligand spin, they almost never flip the Dy^{3+} total angular momentum or nuclear spin.

The measurement thus projects the system onto a nuclear spin eigenstate and realizes a nearly ideal quantum non-demolition readout.

To critically test this interpretation of the experimental data, we follow the approach of Thiele et al. [8] and apply a microwave field to the tunneling junction using a separate microwave antenna [35]. In TbPc_2 this method has been used to drive nuclear spin transitions via the nuclear Stark effect. For this, a field of 50 mT is applied to align the Dy^{3+} moment and suppress the telegraph noise by lifting the degeneracy of the Dy states through the Zeeman interaction (Fig. 4a). The differential conductance of the Kondo peak is then recorded with non-magnetic tips and will still depend on the nuclear spin due to the sensitivity of the Kondo line shape on the nuclear spin state. Next, the radio-frequency (RF) is then ramped up and the tunneling current is monitored. When the RF frequency matches a nuclear spin transition, the nuclear spin changes and the Kondo peak intensity changes due to its dependence on the nuclear spin state. For the ground state ($I_z = 5/2$), dipole transitions at 433.4 MHz and quadrupole transitions at 1149.4 MHz are expected.

Figure 4b shows clear increases in current difference at 435.5 MHz and 447.2 MHz, in good agreement with the predicted dipole transition at 433.4 MHz. The linewidth of the resonance is approximately 3 MHz, comparable to values reported for TbPc_2 molecules in break-junction experiments [36]. Interestingly, the transition splits into two lines. This splitting is attributed to the interaction between the ligand spin and the Dy^{3+} nuclear spin, which produces an additional hyperfine splitting. At higher frequencies also two peaks are observed near the expected quadrupole transition around 1151 MHz. Alternatively,

the two peaks could be due to the split dipole transition from the second excited state to the third. Note that we calibrated the microwave transmission to the STM junction and account for the frequency-dependent transmission in the analysis (see Supplemental Material).

The observed resonance peaks show no measurable dependence on the applied magnetic field. This behavior reflects the very small nuclear Zeeman interaction, which does not shift the resonance frequencies within the magnetic-field range where the Kondo peaks remain observable. Consistently, the same resonances are observed for magnetic fields between 0 and 50 mT and for both non-magnetic and spin-polarized STM tips.

In conclusion, a straightforward method to read the nuclear spin of the ^{163}Dy isotope in $^{163}\text{DyPc}_2$, a prototypical $4f$ single-molecule magnet, is demonstrated using spin-polarized scanning tunneling microscopy. The hyperfine interaction stabilizes the Dy^{3+} magnetic moment and enables its orientation to be determined through spin-polarized tunneling and telegraph-noise measurements, from which nuclear-spin-dependent relaxation times T_1 can be extracted. As the sharp Kondo peaks react on the small energetic changes of the states induced by the nuclear spin state, also the nuclear spin state can be inferred from simple conductance measurements and transitions of the nuclear spin state were detected by nuclear magnetic resonance spectroscopy. This opens up the possibility to combine nuclear spins with relatively fast electronic manipulation and readout without the need for magnetic-field sweeps. More generally, the concept of using a Kondo-screened spin as a probe for an exchange-coupled quantum degree of freedom may be extended to a broad class of systems. We speculate that similar schemes can also be extended to superconducting substrates, in which the split and fully spin-polarized Kondo resonance would turn into a Yu-Shiba-Rusinov (YSR) state [37–39]. The YSR states also offer the advantage that they are typically sharper in energy and thus the changes in the YSR states caused by the nuclear spin state lead to even larger signals.

ACKNOWLEDGMENTS

We acknowledge financial support from the Deutsche Forschungsgemeinschaft (DFG, German Research Foundation) through the Collaborative Research Centre “4f for Future” (CRC 1573, Project 471424360) Project B2 and through Project Wu 349/17-1, as well as fruitful discussions with Wolfgang Wernsdorfer, Luca Kosche and Anja Metelmann.

H.C. and S.G. contributed equally to this work.

EXPERIMENTAL SETUP

The measurements were performed in a home-built ultra-high vacuum (UHV) scanning tunneling microscope (STM) that can operate at a base temperature of approximately 25 mK with an external magnetic field of up to 7 T applied normal to the surface plane [40]. Spin-polarized STM tips were prepared by coating a tungsten (W) tip with antiferromagnetic chromium (Cr) [41, 42]. The out-of-plane spin polarization of the tip was adjusted by varying the thickness of the Cr coating. The Au(111) crystal was cleaned using repeated cycles of Ar⁺ sputtering, followed by annealing at 500 °C. Subsequently, ¹⁶³DyPc₂ molecules were deposited onto the clean Au(111) substrate, which was held at a temperature around 100 K to 120 K, from a Knudsen cell operated at 400 °C under UHV conditions. The substrate was then transferred in situ to the STM. In order to enable the tuning of nuclear transitions with atomic-scale spatial resolution, an RF line was integrated into the STM setup to allow the exact measurement of the molecular response. A schematic of the RF circuit is shown in Fig. 5.

The primary challenge is the transmission of the RF signal from room temperature into the UHV environment and down to dilution temperature, while avoiding additional noise, thermal heating, and mechanical vibrations. The signal path is divided into three sections: firstly, a standard SMA cable with an attenuator located outside the vacuum chamber; secondly, an electrical feed-through; and thirdly, a flexible cable located inside the chamber that terminates in an antenna positioned in close proximity to the junction. Excitation of the junction is thus achieved by the free RF field [35]. It is evident that each transition introduces signal attenuation and reflections, phenomena that becomes more pronounced at higher frequencies.

The RF excitation is provided by an SMB 100A signal generator, while detection of small AC signals is performed using a lock-in amplifier. The lock-in amplifier is responsible for generating the low-frequency (LF) modulation signal, that modulates the RF amplitude. Detection of the systems response (in the tunneling current) to the RF signal is done via the lock-in amplifier. The amplitude modulated RF excitation from the signal generator (100 MHz to 2 GHz) is thus applied to the junction via a frequency dependent transmission function. The transmission calibration process involves the initial selection of an RF amplitude that ensures the response does not saturate, thereby establishing a reference level. Subsequently, frequency-dependent correction factors are determined in order to adjust the applied RF power and compensate for attenuation in the transmission line [43].

The use of a 6 dB attenuator is essential in reducing the internal reflections of signal line. Meanwhile, the RF power applied through the transmission line must be appropriately adjusted to ensure a constant signal is received by the tunneling junction over the entire frequency range. In order to determine the frequency-dependent response of the RF circuit, it is necessary to exploit strongly nonlinear current–voltage characteristics. The following reference systems have been identified as being suitable: a Pb(111) sample with sharp superconducting coherence peaks (compare [35]) or a sharp Kondo resonance FePc molecules on Au(111) [44]. By monitoring the change of these nonlinear features as a function of RF frequency and amplitude, the effective RF amplitude at the junction can be calibrated. The present procedure is designed to compensate for the intrinsic frequency dependence of the transmission line, thereby enabling quantitative comparison of frequency-dependent effects in the molecules being studied.

As seen in Fig. 6b, the upper panel is related to the transmission near 433 MHz. In this frequency range, the signal displays a double peak around 440 MHz and a single peak near 490 MHz. Comparison with the calibration factor obtained from the Pb reference reveals that the calibration curve remains nearly constant around 440 MHz, while it shows a peak of a similar shape at 490 MHz. We therefore attribute the double peak near 440 MHz to a transitional peak. This is because it does not coincide with any structure in the calibration file. In contrast, the peak at 490 MHz matches a feature in the calibration factor and is thus assigned to imperfect calibration rather than to an intrinsic transition. A similar behavior is seen for the second transition near 1050 MHz in the lower panel of the figure. At this frequency, the calibration factor remains constant at the position of the measured transition peaks, thereby validating their physical origin. However, the calibration curve displays a maximum at 1130 MHz, which is also observed in the transmission measurement. Therefore, this feature is attributed to transmission-line interference rather than an intrinsic transition.

The calibration using the sharp Kondo resonance observed for FePc molecules adsorbed on Au(111) has the advantage, that no change of sample was necessary between calibration and measurement. For this purpose, FePc molecules were co-deposited on the Au(111) crystal together with ¹⁶³DyPc₂, and as shown in Fig. 7a, two cross-shaped molecules are visible, with the higher one exhibiting an apparent height of 186 pm. These characteristics are attributed to FePc molecules on the surface. Experiments show that FePc adsorbs on Au(111) in different configurations, commonly referred to as on-top and bridge sites [44]. These configurations exhibit

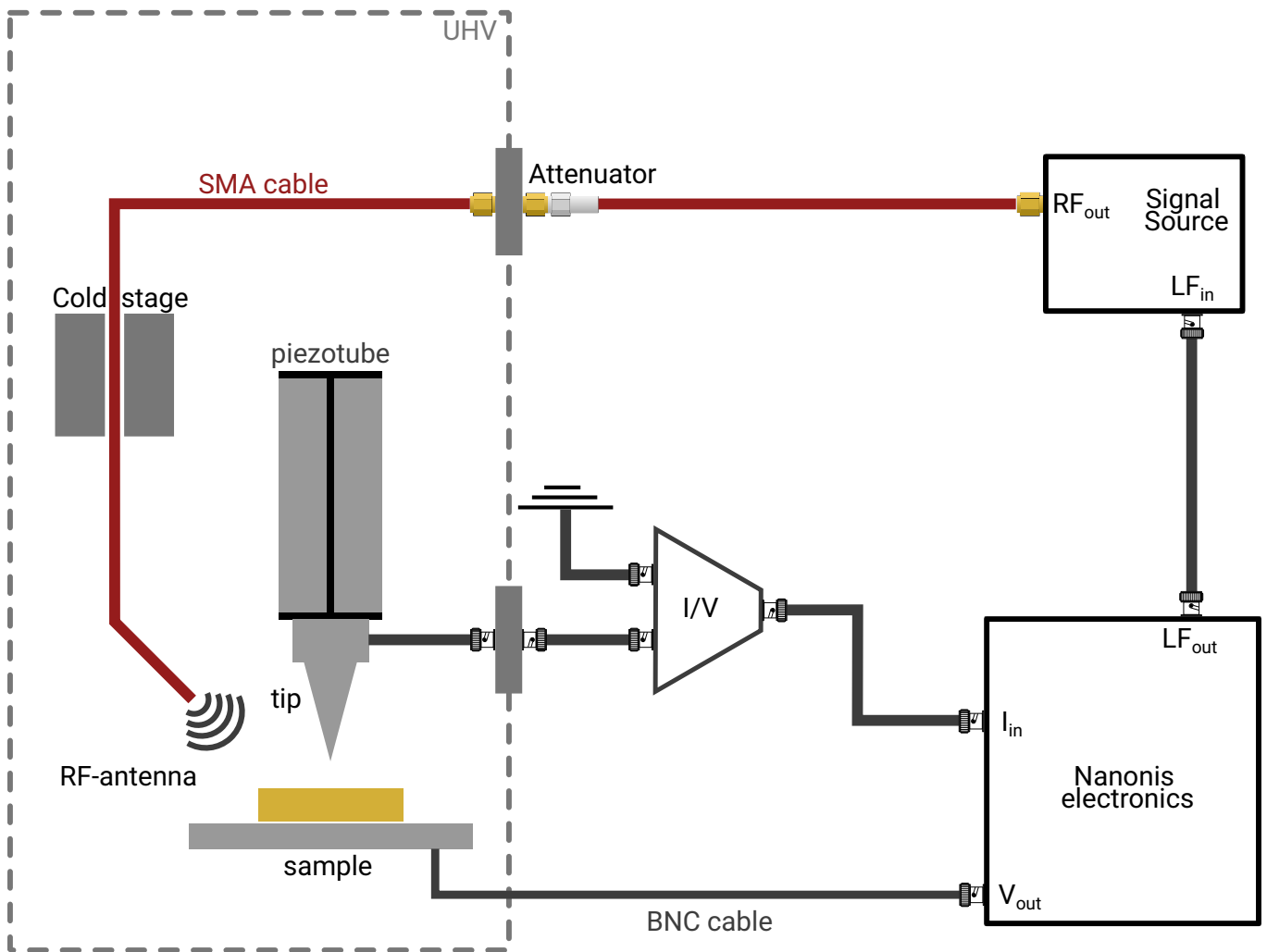


Figure 5. The configuration comprises an STM tip positioned above the sample and controlled by Nanonis electronics. For RF measurements, an RF antenna is coupled to the cryostat, thereby enabling cooling to dilution temperatures. The antenna is connected to the UHV chamber through a feedthrough and a 6 dB attenuator. The RF signal is generated by an external source and demodulated within the Nanonis system.

distinct spectroscopic signatures. The configuration associated with a sharp dip in the differential conductance spectrum, shown in Fig. 7b, is consistent with the Kondo feature that was reported for the on-top adsorption site. A second option for calibration was given by sharp Kondo peak from ontop site positioned FePc molecules.

LIFETIMES

To analyze the jumps in z-position over time for the measured signal, we divided the signal in three colored sections where each has an upper and lower state. For each state we determined the dwell times defined as the duration for which the system remains in this state before it jumps to the corresponding level. A jump was counted when the signal stayed longer than two consecutive data points below the midpoint value in this section. Transi-

tions were not evaluated across section boundaries. From these dwell times, the population fraction was evaluated assuming that the remaining population after the i -th event dropped to $(N - i)/N$ where N represents total event count. Subsequently, the data were fitted using an exponential decay of the form

$$f(t) = A \cdot e^{-\frac{t}{\tau}} \quad (2)$$

where τ represents the mean lifetime of the respective state.

The fitted decays with the corresponding lifetimes can be seen in figure 8. The red region has the fastest switching rate and a nearly balanced population, though the upper state is slightly more occupied. This behavior suggests vicinity to an avoided level crossing, a claim supported by lifetime analysis. Both states decay exponentially with mean lifetimes below one second. The population asymmetry is also reflected in the upper state's

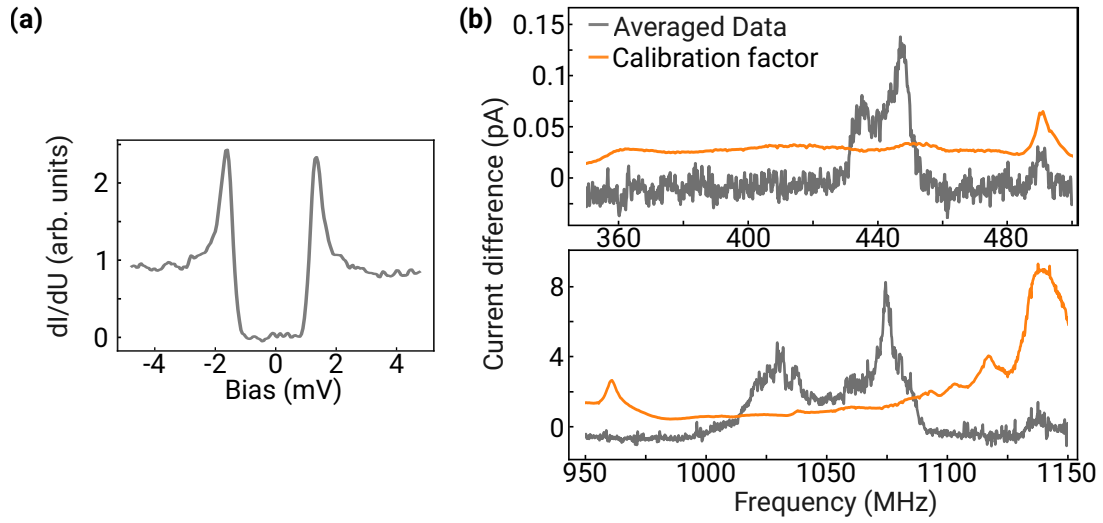


Figure 6. Transmission line calibration on a Pb(111) crystal (a) Spectroscopic measurement of the superconducting gap of a Pb(111) crystal. The coherence peaks of a superconducting gap of a Pb(111) crystal was used to calibrate our transmission line. The spectra was measured using a lock-in modulation of $U_{\text{mod}} = 100 \mu\text{V}$, feedback conditions of $U = 5 \text{ mV}$, $I = 100 \text{ pA}$ at a temperature of $T = 800 \text{ mK}$. (b) A comparison of the resulting calibration factor with the independently measured transmission signal for both transitions is shown. The data in the upper panel were acquired with feedback parameters $U = 150 \mu\text{V}$, $I = 20 \text{ pA}$, and an RF amplitude of $V_{\text{RF}} = 350 \text{ mV}$. The lower panel was recorded with the following feedback parameters: $U = 75 \mu\text{V}$, $I = 20 \text{ pA}$, and $V_{\text{RF}} = 350 \text{ mV}$.

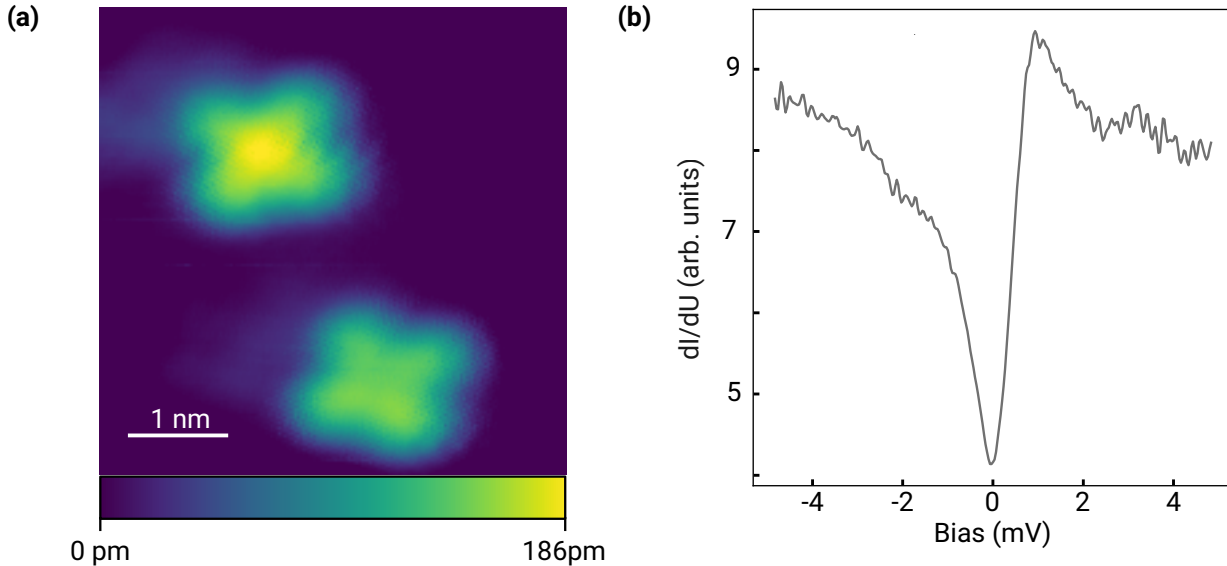


Figure 7. Scanning tunneling microscopy and scanning tunneling spectroscopy (STS) were used to investigate FePc molecules on an Au(111) surface. (a) An STM image (34 pA , $500 \mu\text{V}$) showing two cross-shaped FePc molecules adsorbed on the Au(111) surface. (b) STS spectrum (5 mV , 100 pA , Lockin: $500 \mu\text{V}$, 3230 Hz) acquired on the molecular center exhibiting a sharp dip feature near zero bias that is consistent with a Kondo resonance for ontop site FePc molecules [44].

longer lifetime. In the green area, the switching rate is lower and the lower state shows a higher, but still similar, population. Similar behavior is displayed by the lifetime fits, which show exponential decay and mean lifetimes slightly above 1 s, with the more populated lower state having a slightly longer lifetime. The slowest switching rate and a strong asymmetry toward the lower state are

shown by the blue region. Despite the reduced number of events, an exponential decay model can still be fitted. The mean lifetimes are $\tau = 6.65 \text{ s}$ for the upper state and $\tau = 55 \text{ s}$ for the lower state, which is consistent with the observed population imbalance. In general, an increase in population asymmetry is associated with an increase in lifetime.

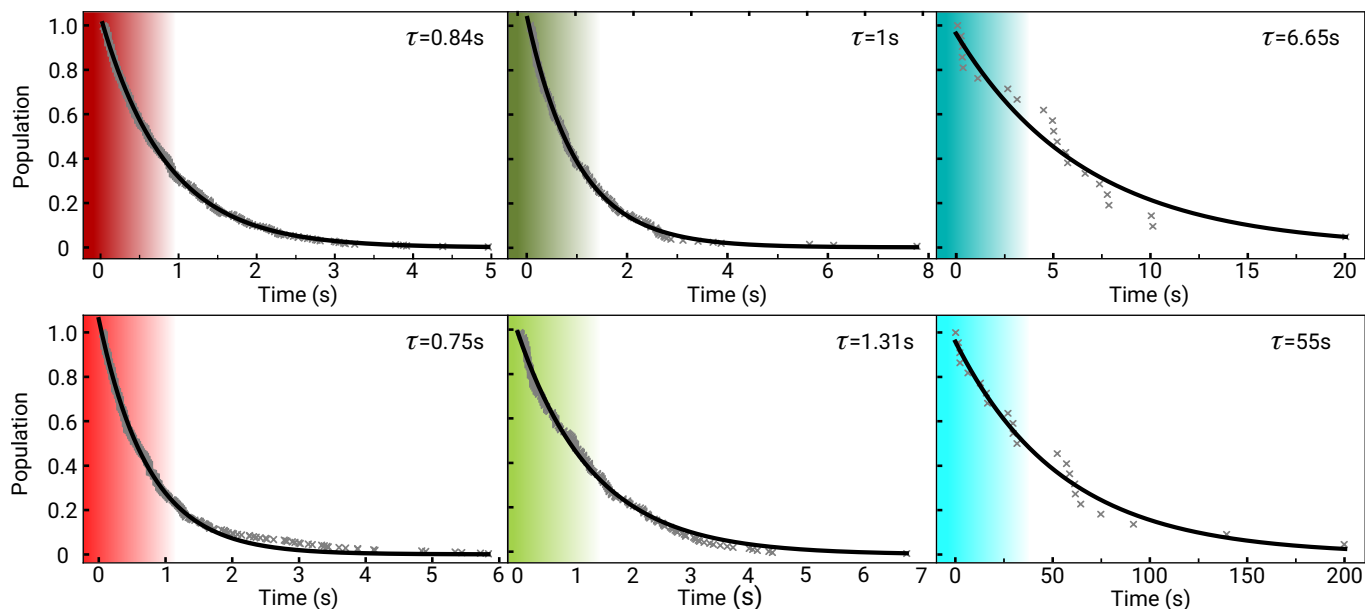


Figure 8. Exponential decay of the states representing the lifetime. For each colored section the population for upper and lower state over time was plotted.

EFFECTIVE SPIN HAMILTONIAN PARAMETERS

The following is a summary of the parameters used in the simulations and their sources. The anisotropy constants for the crystal field Hamiltonians were obtained from private communication with Eufemio [45]. The hyperfine and quadrupole parameters a and P were taken from the literature [19] and converted from the EasySpin convention to the Hamiltonian definition given by equation 1.

Table I. Hamiltonian parameters

Parameter	Value (cm^{-1})
B_2^0	$376.02 \cdot (-2/9/35)$
B_2^2	$0.024 \cdot (-2/9/35)$
B_4^0	$-142.7 \cdot (-8/11/45/273)$
B_4^4	$2.92 \cdot (-8/11/45/273)$
B_6^0	$25.77 \cdot (4/11^2/13^2/3^3/7)$
B_6^4	$2.35 \cdot (4/11^2/13^2/3^3/7)$
A	0.0051
P	0.00467

GENERAL SYNTHETIC REMARKS

All reagents and solvents (analytical grade) were purchased from commercial suppliers (Sigma-Aldrich) and used as received unless otherwise stated.

Isotopically enriched dysprosium oxide starting material, ($^{163}\text{Dy}_2\text{O}_3$ (94.6 %)) was purchased from BuyIsotope, Sweden. The oxide lanthanide was then converted to the

acetylacetonate counterpart employing published procedures [19, 46].

All manipulations were conducted using standard laboratory practices.

Synthesis. The synthesis of $[\text{DyPc}_2]^0$ and $[\text{Dy}^{163}\text{Dy}_2]^0$ was accomplished by templating reactions, starting from a mixture of the phthalonitrile precursor *o*-dicyanobenzene and the ytterbium acetylacetonate $\text{Dy}(\text{acac})_3 \cdot n\text{H}_2\text{O}$ or $^{163}\text{Dy}(\text{acac})_3 \cdot n\text{H}_2\text{O}$, in the presence of a strong base [e.g., 1,8-diazabicyclo[5,4,0]undec-7-ene (DBU)] and high-boiling solvents, such as pentanol according to a procedure established earlier [19, 47] and analytical data confirmed its intact structure (see Fig. S1 and S2). By means of additional radial chromatography on silica gel followed by recrystallization from chloroform-hexane mixture, analytically pure powder samples were achieved.

The green fraction was collected and recrystallized from chloroform/hexane to afford a black powder of $[\text{DyPc}_2]^0$. UV/Vis (DCM) (nm): 280, 321, 4614, 599, 665; HRMS (MALDI-ToF mass spectra for, positive mode): m/z calcd. for $[\text{M}]^+$ $\text{DyC}_{64}\text{H}_{32}\text{N}_{16}$ 1188.2400 Da; found 1188.2367 Da. For ^{163}Dy $\text{C}_{64}\text{H}_{32}\text{N}_{16}$: UV/Vis (DCM) (nm): 280, 321, 4614, 599, 665; HRMS (MALDI-ToF mass spectra for, positive mode): m/z calcd. for $[\text{M}]^+$ 1186.97424 Da; found 1187.02006 Da.

Characterization UV-visible-NIR spectra were measured on a Varian Cary 500 Scan UV/vis/NIR spectrophotometer by using a 1 cm optical path length quartz cell. MALDI-ToF spectra were recorded on a Waters SYNAPTTM-G2-Plattform in the positive ion mode.

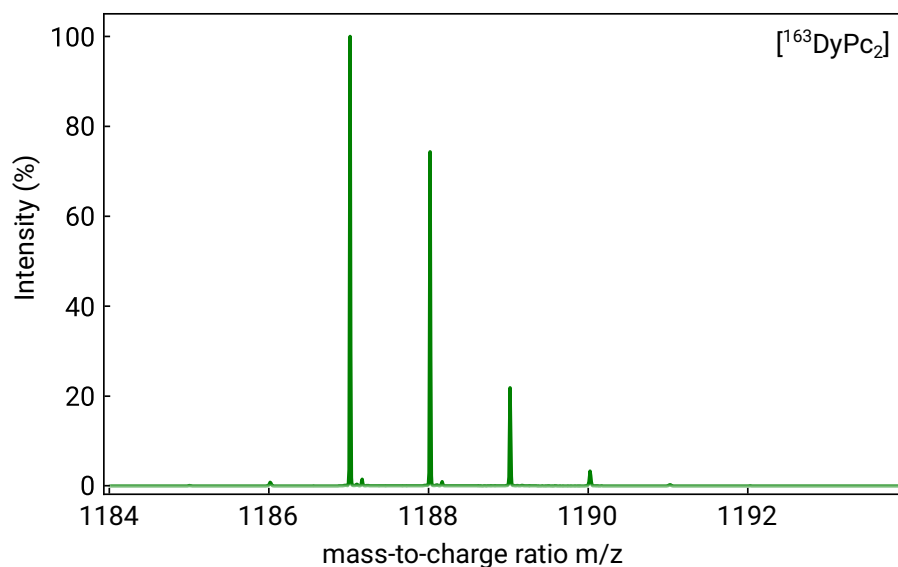


Figure 9. The positive MALDI mass spectra in a zoomed range for the intensity peak of the Isotope $[^{163}\text{DyPc}_2]^0$.

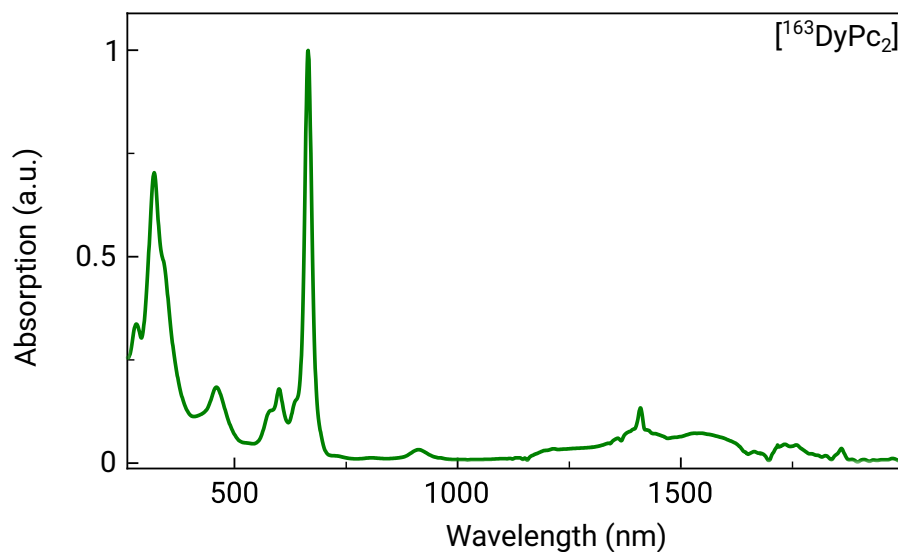


Figure 10. The UV/vis/nIR absorption spectrum of $[^{163}\text{DyPc}_2]^0$ is similar to the neutral green form of $[\text{LnPc}_2]^0$ spectra [48] with the most intense band - the Q-band - at 672 nm. In the near-infrared region two main bands are observed at about 906 nm and 1300 nm to 1800 nm. The shorter wavelength band is related to the radical part and attributed to the $1e_g \rightarrow a_1u$ transition; the lower-energy band is assigned to an intramolecular charge transfer (CTI). Those signals are the fingerprints of the neutral species $[\text{LnPc}_2]^0$ and, thus, confirm their nature. All the near-infrared bands disappear upon reduction by hydrazine hydrate (1% vv).

-
- * These authors contributed equally to this work.; simon.gerber@kit.edu
- [1] M. Atzori and R. Sessoli, *Journal of the American Chemical Society* **141**, 11339 (2019).
 - [2] E. Moreno-Pineda, C. Godfrin, F. Balestro, W. Wernsdorfer, and M. Ruben, *Chemical Society Reviews* **47**, 501 (2018).
 - [3] W. Wernsdorfer and M. Ruben, *Advanced Materials* **31**, 1806687 (2019).
 - [4] C. A. Goodwin, F. Ortu, D. Reta, N. F. Chilton, and D. P. Mills, *Nature* **548**, 439 (2017).
 - [5] M. Shiddiq, D. Komijani, Y. Duan, A. Gaita-Ariño, E. Coronado, and S. Hill, *Nature* **531**, 348 (2016).
 - [6] A. Lodi Rizzini, C. Krull, T. Balashov, J. J. Kavich, A. Mugarza, P. S. Miedema, P. K. Thakur, V. Sessi, S. Klyatskaya, M. Ruben, S. Stepanow, and P. Gambardella, *Phys. Rev. Lett.* **107**, 177205 (2011).
 - [7] S. Thiele, F. Balestro, R. Ballou, S. Klyatskaya, M. Ruben, and W. Wernsdorfer, *Science* **344**, 1135 (2014).
 - [8] S. Thiele, R. Vincent, M. Holzmann, S. Klyatskaya, M. Ruben, F. Balestro, and W. Wernsdorfer, *Phys. Rev. Lett.* **111**, 037203 (2013).
 - [9] D. N. Woodruff, R. E. P. Wimpenny, and R. A. Layfield, *Chem. Rev.* **113**, 5110 (2013).
 - [10] F.-S. Guo, B. M. Day, Y.-C. Chen, M.-L. Tong, A. Mansikkamäki, and R. A. Layfield, *Science* **362**, 1400 (2018).
 - [11] S. Müllegger, S. Tebi, A. K. Das, W. Schöfberger, F. Faschinger, and R. Koch, *Phys. Rev. Lett.* **113**, 133001 (2014).
 - [12] R. Vincent, S. Klyatskaya, M. Ruben, W. Wernsdorfer, and F. Balestro, *Nature* **488**, 357 (2012).
 - [13] T. Komeda, H. Isshiki, J. Liu, Y.-F. Zhang, N. Lorente, K. Katoh, B. K. Breedlove, and M. Yamashita, *Nat. Commun.* **2**, 1 (2011).
 - [14] T. Komeda, K. Katoh, and M. Yamashita, *Prog. Surf. Sci.* **89**, 127 (2014).
 - [15] B. Warner, F. El Hallak, N. Atodiresei, P. Seibt, H. Prüser, V. Caciuc, M. Waters, A. J. Fisher, S. Blügel, J. van Slageren, and C. F. Hirjibehedin, *Nat. Commun.* **7**, 12785 (2016).
 - [16] L. K. Grover, *Physical Review Letters* **79**, 325 (1997).
 - [17] M. N. Leuenberger and D. Loss, *Nature* **410**, 789 (2001).
 - [18] C. Godfrin, A. Ferhat, R. Ballou, S. Klyatskaya, M. Ruben, W. Wernsdorfer, and F. Balestro, *Phys. Rev. Lett.* **119**, 187702 (2017).
 - [19] E. Moreno-Pineda, M. Damjanović, O. Fuhr, W. Wernsdorfer, and M. Ruben, *Angew. Chem. Int. Ed.* **56**, 9915 (2017).
 - [20] K. Kasuga, M. Tsutsui, R. C. Petterson, K. Tatsumi, N. Van Opdenbosch, G. Pepe, and E. F. Meyer, *J. Am. Chem. Soc.* **102**, 4835 (1980).
 - [21] M. Moussavi, A. De Cian, J. Fischer, and R. Weiss, *Inorg. Chem.* **27**, 1287 (1988).
 - [22] N. Koike, H. Uekusa, Y. Ohashi, C. Harnood, F. Kitamura, T. Ohsaka, and K. Tokuda, *Inorg. Chem.* **35**, 5798 (1996).
 - [23] N. Ishikawa, M. Sugita, T. Okubo, N. Tanaka, T. Iino, and Y. Kaizu, *Inorg. Chem.* **42**, 2440 (2003).
 - [24] N. Ishikawa, M. Sugita, T. Ishikawa, S.-y. Koshihara, and Y. Kaizu, *J. Am. Chem. Soc.* **125**, 8694 (2003).
 - [25] T. Frauhammer, H. Chen, T. Balashov, G. Derenbach, S. Klyatskaya, E. Moreno-Pineda, M. Ruben, and W. Wulfhekel, *Physical Review Letters* **127** (2021).
 - [26] I. I. Vrubel, A. A. Pervishko, H. Herper, B. Brena, O. Eriksson, and D. Yudin, *Physical Review B* **101**, 125106 (2020).
 - [27] K. von Bergmann, M. Ternes, S. Loth, C. P. Lutz, and A. J. Heinrich, *Physical Review Letters* **114**, 076601 (2015).
 - [28] M. Bagchi, T. Y. Tounsi, A. Safeer, C. van Efferen, A. Rosch, T. Michely, W. Jolie, T. A. Costi, and J. Fischer, *Phys. Rev. Lett.* **133**, 246701 (2024).
 - [29] M. Julliere, *Physics Letters A* **54**, 225 (1975).
 - [30] K. Stevens, *Proc. Phys. Soc. A* **65**, 209 (1952).
 - [31] T. Miyamachi, T. Schuh, T. Märkl, C. Bresch, T. Balashov, A. Stöhr, C. Karlewski, S. André, M. Marthaler, M. Hoffmann, M. Geilhufe, S. Ostanin, W. Hergert, I. Mertig, G. Schön, A. Ernst, and W. Wulfhekel, *Nature* **503**, 242 (2013).
 - [32] T. Balashov, C. Karlewski, T. Märkl, G. Schön, and W. Wulfhekel, *Phys. Rev. B* **97**, 024412 (2018).
 - [33] N. Ishikawa, M. Sugita, and W. Wernsdorfer, *Angeordnete Chemie International Edition* **44**, 2931 (2005).
 - [34] M. Ternes, *New J. Phys.* **17**, 063016 (2015).
 - [35] O. Peters, N. Bogdanoff, S. Acero González, L. Melischeck, J. R. Simon, G. Reecht, C. B. Winkelmann, F. von Oppen, and K. J. Franke, *Nature Physics* **16**, 1222 (2020).
 - [36] C. Godfrin, S. Thiele, A. Ferhat, S. Klyatskaya, M. Ruben, W. Wernsdorfer, and F. Balestro, *ACS Nano* **11**, 3984 (2017).
 - [37] L. Yu, Wu Li Hsueh Pao (China) Supersedes Chung-Kuo Wu Li Hsueh For English translation see *Chin. J. Phys. (Peking) (Engl. Transl.)* **Vol: 21** (1965).
 - [38] H. Shiba, *Progress of Theoretical Physics* **40**, 435 (1968), <https://academic.oup.com/ptp/article-pdf/40/3/435/5185550/40-3-435.pdf>.
 - [39] A. I. Rusinov, *JETP Lett. (USSR) (Engl. Transl.)*, 9: 85-7(Jan. 20, 1969). (1969).
 - [40] T. Balashov, M. Meyer, and W. Wulfhekel, *Rev. Sci. Instrum.* **89**, 113707 (2018).
 - [41] A. Kubetzka, M. Bode, O. Pietzsch, and R. Wiesendanger, *Phys. Rev. Lett.* **88**, 057201 (2002).
 - [42] O. Pietzsch, A. Kubetzka, M. Bode, and R. Wiesendanger, *Phys. Rev. Lett.* **92**, 057202 (2004).
 - [43] M. Hervé, M. Peter, and W. Wulfhekel, *Applied Physics Letters* **107**, 093101 (2015).
 - [44] E. Minamitani, N. Tsukahara, D. Matsunaka, Y. Kim, N. Takagi, and M. Kawai, *Physical Review Letters* **109**, 086602 (2012).
 - [45] E. Moreno-Pineda, (2021), institute for Quantum Materials and Technologies, Karlsruhe. Personal communication.
 - [46] J. G. Stites, C. N. McCarty, and L. L. Quill, *Journal of the American Chemical Society* **70**, 3142 (1948).
 - [47] F. Branzoli, P. Carretta, M. Filibian, M. J. Graf, S. Klyatskaya, M. Ruben, F. Coneri, and P. Dhakal, *Phys. Rev. B* **82**, 134401 (2010).
 - [48] D. Markovitsi, T.-H. Tran-Thi, R. Even, and J. Simon, *Chemical Physics Letters* **137**, 107 (1987).